2D and 3D reconstructions in acousto-electric tomography

2011 Inverse Problems 27 055013

(http://iopscience.iop.org/0266-5611/27/5/055013)

Inverse Problems **27** (2011) 055013 (21pp) doi:10.1088/0266-5611/27/5/055013

2D and 3D reconstructions in acousto-electric tomography

Peter Kuchment[1] **and Leonid Kunyansky**[2]

[1] Department of Mathematics, Texas A&M University, College Station, TX 77843, USA
[2] Department of Mathematics, University of Arizona, Tucson, AZ 85721, USA

E-mail: kuchment@math.tamu.edu and leonk@math.arizona.edu

Received 2 December 2010, in final form 21 February 2011
Published 18 April 2011
Online at stacks.iop.org/IP/27/055013

Abstract

We propose and test stable algorithms for the reconstruction of the internal conductivity of a biological object using acousto-electric measurements. Namely, the conventional impedance tomography scheme is supplemented by scanning the object with acoustic waves that slightly perturb the conductivity and cause the change in the electric potential measured on the boundary of the object. These perturbations of the potential are then used as the data for the reconstruction of the conductivity. The present method does not rely on 'perfectly focused' acoustic beams. Instead, more realistic propagating spherical fronts are utilized, and then the measurements that would correspond to perfect focusing are synthesized. In other words, we use *synthetic focusing*. Numerical experiments with simulated data show that our techniques produce high-quality images, both in 2D and 3D, and that they remain accurate in the presence of high-level noise in the data. Local uniqueness and stability for the problem also hold.

(Some figures in this article are in colour only in the electronic version)

1. Introduction

Electrical impedance tomography (EIT) is a harmless and inexpensive imaging modality, with important clinical and industrial applications. It aims to reconstruct the internal conductivity of a body using boundary electric measurements (see, e.g., [4, 6, 8, 9]). It is well known that, regretfully, it suffers from inherent low resolution and instability. To bypass this difficulty, various versions of a new hybrid technique, sometimes called acousto-electric tomography (AET), have been introduced recently [3, 7, 16, 25]. (See also [12] for a different way to recover the conductivity using combination of ultrasound and EIT.) AET utilizes the electro-acoustic effect, i.e. occurrence of small changes in tissue conductivity as the result of applied acoustic pressure [20, 21]. Although the effect is small, it was shown in [25] that it provides a signal that can be used for imaging the conductivity. It has been understood [3, 7, 16] that

if one could apply concentrated pressure at a given point inside the body and then measure the resulting change in impedance measurements, the knowledge of the perturbation point would have a stabilizing effect on the reconstruction in otherwise highly unstable EIT. It has been proposed to use a tightly focused ultrasound beam as a source of such point-like acoustic pressure [3]. However, since perfect focusing of acoustic waves is hard to achieve in practice (see, e.g., [14]), an alternative *synthetic focusing* approach was developed in [16]. Namely, the medium is perturbed by a series of more realistic propagating spherical acoustic fronts with centers lying outside of the object (other options, e.g. plane waves or monochromatic spherical waves could also be used [16]). The resulting changes in the values of electric potential on the boundary of the object are recorded. Then the data that would have been collected, if perfect focusing were possible, are synthesized mathematically. Such synthesis happens to be equivalent to the well-established inversion in the so-called thermoacoustic tomography (see, e.g., the surveys [15, 23, 24]). Of course, for accurate synthesis the acoustic properties of the medium should be known. In breast imaging, for example, the speed of sound in the tissue can be well approximated by a constant, and application of AET in this area looks very promising. In the inhomogeneous medium, synthetic focusing is possible if its acoustic parameters are reconstructed beforehand (for example, using methods of ultrasound tomography). The results of the first numerical experiments presented in [16] confirm the feasibility of synthetic focusing.

In this paper, we describe a stable and efficient local algorithm for the AET problem. From the formulas we present, one can easily infer the local uniqueness and stability of the reconstruction. However, after this work was performed, the authors have learned of a paper [7], some results of which (propositions 2.1 and 2.2) imply uniqueness and Lipschitz stability in a similar setting (see also [5] for the presentation of such a local result). We thus address these issues only briefly here.

The presented algorithm involves two steps. First, it synthesizes the data corresponding to perfectly focused ultrasound perturbations from the data obtained using more realistic spherical waves. Here the known smallness of the acousto-electric effect [20, 21, 25] is crucial, since it permits linearization with respect to the acoustic perturbation and thus makes synthetic focusing possible. Second, the algorithm reconstructs the conductivity from the data corresponding to perfectly focused perturbations. This second step, from measured data to the conductivity, is nonlinear. We develop a linearized algorithm, assuming that the conductivity is close to a known one. The numerical examples that we provide show that this approach works surprisingly well even when the initial guess is very distinct from the correct conductivity. One can apply iterations for further improvements.

To the best of the authors' knowledge, the first step of our method (synthetic focusing) has not been discussed previously in works on AET, except for a brief description in our papers [16, 18]. On the other hand, three different approaches to reconstruction using a perfectly focused beam (the second step of our algorithm) have recently been proposed [3, 7, 16, 18]. Let us thus indicate the differences with these recent works.

In [3], two boundary current profiles were used and the problem of reconstructing the conductivity was reduced to a numerical solution of a (nonlinear) PDE involving the 0-Laplacian. In [16, 18], by a rather crude approximation, we reduced the reconstruction problem to solving a transport equation (a single current was used). Unfortunately, in the case of noisy measurements, the errors tend to propagate along characteristics, producing unpleasant artifacts in the images, which can be reduced by iterations. There is also a version of this procedure that involves an elliptic equation and thus works better. In [7], two current profiles are used in 2D (three profiles in 3D); the problem is reduced to a minimization problem, which is then solved numerically. In this paper, we also use two currents in 2D

(two or three in 3D) and, in the second step, we utilize the same data as in [7]. Unlike [7], in our work the reconstruction problem is solved, under the assumption that the conductivity is close to some initial guess, by a simple algorithm, which even in the first step produces good images, improved further by iterations. The algorithm essentially boils down to solving a Poisson equation. Numerical experiments show high-quality reconstructions, quite accurate even in the presence of very significant noise. Reconstructions remain accurate when the true conductivity differs significantly from the initial guess.

The rest of the paper is organized as follows. Section 2 contains the formulation of the problem. It also addresses the focusing issue. Section 3 describes the reconstruction algorithm, whose stability is discussed in section 4. Numerical implementation and results of the reconstruction from simulated data in 2D are described in section 5. Sections 6 and 7 address the 3D case. Section 8 is devoted to final remarks and conclusions.

2. Formulation of the problem

Let $\sigma(x)$ be the conductivity of the medium within a bounded region Ω. Then the propagation of the electrical currents through Ω is governed by the divergence equation

$$\nabla \cdot \sigma(x)\nabla u(x) = 0, \quad x \in \Omega, \tag{1}$$

or, equivalently

$$\Delta u(x) + \nabla u(x) \cdot \nabla \ln \sigma(x) = 0, \tag{2}$$

where $u(x)$ is the electric potential. Let us assume that $\sigma - 1$ is compactly supported within the region Ω, and that $\sigma(x) = 1$ in the neighborhood of the boundary $\partial\Omega$. We also assume that the currents $J = \sigma \frac{\partial}{\partial n} u(x)$ through the boundary are fixed and the values of the potential u are measured on the boundary $\partial\Omega$.

The acoustic wave propagating through the object slightly perturbs the conductivity $\sigma(x)$. Following the observations made in [20, 21], we assume that the perturbation is proportional to the local value of the conductivity; thus, the perturbed conductivity $\sigma^{\text{new}}(x)$ equals $\sigma(x)\exp(\eta(x))$, where the perturbation exponent $\eta(x)$ is such that $|\eta(x)| \ll 1$ and is compactly supported. Let $u^{\text{new}}(x) = u(x) + w_\eta(x)$ be the potential corresponding to the perturbed conductivity $\sigma^{\text{new}}(x)$ and $w_\eta(x)$ be the perturbation thereof. By substituting these perturbed values into (2), one obtains

$$\Delta[u(x) + w_\eta(x)] + \nabla[u(x) + w_\eta(x)] \cdot \nabla[\ln \sigma(x) + \eta(x)] = 0. \tag{3}$$

Further, by neglecting the second-order terms (in η) and by subtracting (2) from (3), we arrive at the following equation:

$$\Delta w_\eta(x) + \nabla w_\eta(x) \cdot \nabla \ln \sigma(x) = -\nabla u(x) \cdot \nabla \eta(x). \tag{4}$$

Finally, by multiplying (4) by $\sigma(x)$, we find that $w_\eta(x)$ satisfies the equation

$$\nabla \cdot \sigma(x)\nabla w_\eta(x) = -\sigma(x)\nabla u(x) \cdot \nabla \eta(x) \tag{5}$$

subject to the homogeneous Neumann boundary conditions. Since the values of $u(x)$ and $u^{\text{new}}(x)$ are measured on the boundary, the Dirichlet data for $w_\eta(x)$ are known. It will be sufficient for our purposes to measure a certain functional of the boundary values of $w_\eta(x)$. Let us fix a function $I(z)$ defined on $\partial\Omega$, and define the corresponding measurement functional $M_I(\eta)$ as follows:

$$M_{I,J}(\eta) := \int_{\partial\Omega} w_\eta(z) I(z)\, \mathrm{d}z. \tag{6}$$

Here the subscript J on the left is a reminder of the dependence of w on the current J. The function $I(z)$ does not have to be a function in the classical sense; it may also be chosen to be a distribution, for example, a sum of delta functions. In the latter case, it would model measurements obtained by a set of point-like electrodes. Since the data corresponding to all electrodes would then be added together, the noise sensitivity of such a scheme is quite low, and our numerical experiments (not presented here) confirm that.

Our goal is to reconstruct $\sigma(x)$ from measurements of $M_{I,J}(\eta)$ corresponding to a sufficiently rich set of perturbations $\eta(x)$ in (5).

The simplest case is when one can achieve perfect focusing, and thus $\eta_y(x) \approx C\delta(x-y)$, where the point y scans through Ω. Then the reconstruction needs to be performed from the values

$$M_{I,J,\delta}(y) := \int_{\partial\Omega} w_{\eta_y,J}(z) I(z)\, \mathrm{d}z.$$

However, this assumption of perfect focusing is unrealistic [14]. More realistic are, for instance, mono-chromatic planar or spherical waves, or spreading spherical fronts. We assume here that ideal point-like transducers are excited by an infinitesimally short electrical pulse. If we assume (without loss of generality) that the speed of sound equals 1, the acoustic pressure $W_{t,z}(x)$ generated by a transducer placed at point z (outside Ω) solves the following initial value problem for the wave equation:

$$\begin{cases} \Delta_x W_{t,z}(x) = \dfrac{\partial^2}{\partial t^2} W_{t,z}(x), \quad x \in \mathbb{R}^3, \quad t \in [0,\infty) \\ W_{0,z}(x) = \delta(|x-z|), \\ \dfrac{\partial}{\partial t} W_{0,z}(x) = 0. \end{cases}$$

The solution of this problem is well known [22]:

$$W_{t,z}(x) = \frac{\partial}{\partial t}\left(\frac{\delta(t-|x-z|)}{4\pi t}\right); \tag{7}$$

it has the form of the propagating spherical front with the radius t centered at z. (The time derivative of the δ function in (7) results naturally from the δ excitation of the transducer; the spherical waves we used in [16] can be obtained by anti-differentiation of the signal corresponding to (7).)[3]

The perturbation $\eta_{t,z}(x)$ of the conductivity caused by the propagating front $W_{t,z}(x)$ equals $\eta_0 W_{t,z}(x)$, where η_0 is some small fixed proportionality constant (reflecting the smallness of the acousto-electric effect). The corresponding measurements are then (after factoring out η_0)

$$M_{I,J}(t,z) := \int_{\partial\Omega} w_{W_{t,z},J}(z) I(z)\, \mathrm{d}z. \tag{8}$$

Due to the linear dependence of the measurements on the acoustic perturbation η, one can try to perform a 'basis change' type of calculation, which would produce the 'focused' data $M_{I,J,\delta}(y)$ from the more realistic 'non-focused' measurements $M_{I,J}(t,z)$. In particular, as is explained in [16, 18], if one knows the data (8) for all $t \in [0,\infty]$ and $z \in \Sigma$ (where Σ is a closed curve (surface in 3D) surrounding Ω), then $M_{I,J,\delta}(y)$ can be reconstructed by methods of thermoacoustic tomography. In particular, if Σ is a sphere, circle, cylinder, or a surface of a cube, explicit inversion formulas exist that can recover $M_{I,J,\delta}(y)$ (see [15]). For general closed surfaces, other efficient methods exist (e.g., time reversal). This transformation is known to be

[3] Other 'bases' of waves, e.g. radial mono-chromatic, or planar could also be used [16].

stable. In fact, as will be explained below, in the version of synthetic focusing used here, it is smoothing.

We thus assume that $M_{I,J,\delta}(y)$ are known for all $y \in \Omega$ (e.g. they are obtained by synthetic focusing or by direct measurements). For our purposes it will be sufficient to use only two functions $I_1(z)$ and $I_2(z)$ as both the current patterns and the weights in functionals (6). We thus measure or synthesize the following values:

$$M_{i,j}(y) := \int_{\partial\Omega} w_{\eta_y, I_i}(z) I_j(z)\, \mathrm{d}z, \qquad i, j = 1, 2. \tag{9}$$

We now interpret these data in a different manner. Namely, let $u_j(x)$, $j = 1, 2$, be the solutions of (1) corresponding to the boundary currents (i.e. Neumann data) I_j. Then

$$\nabla \cdot \sigma(x) \nabla w_{j,\delta_y}(x) = -\sigma(y) \nabla u_j(y) \cdot \nabla \delta(x - y). \tag{10}$$

Since

$$M_{i,j} = \int_{\partial\Omega} w_i(z) I_j(z)\, \mathrm{d}z,$$

equation (10) and the divergence theorem lead to the formula

$$M_{i,j}(x_0) = \sigma(x_0) \nabla u_i(x_0) \cdot \nabla u_j(x_0). \tag{11}$$

Thus, for any interior point $x \in \Omega$ and any two current profiles I_j, $j = 1, 2$, on the boundary, the values of expressions (11) can be extracted from the measured data.

Our goal now is to try to recover the conductivity from these values. The same problem in 2D was addressed in [7], but our approach to reconstruction is different.

3. Reconstructing the 2D conductivity from focused data using two currents

We will assume here availability of the measurement data $M_{I,J}(x)$ for all $x \in \Omega$, no matter whether they were obtained by applying focused beams, or by synthetic focusing. We will consider now the situation where the conductivity $\sigma(x)$ is considered to be a (relatively) small perturbation of a known benchmark conductivity $\sigma_0(x)$:

$$\sigma(x) = \sigma_0(x)(1 + \varepsilon\rho(x)), \tag{12}$$

where $\varepsilon \ll 1$ and $\rho = 0$ near the boundary of the domain. (Numerical experiments show that our method yields quite accurate reconstructions even when the true conductivity differs significantly from the initial guess σ_0.)

It will also be assumed that two distinct current patterns I_j, $j = 1, 2$, on the boundary are fixed, and the two resulting potentials u_j, $j = 1, 2$, with the benchmark conductivity σ_0,

$$\nabla \cdot \sigma_0(x) \nabla u_j(x) = 0,$$

correspond to the two prescribed sets of boundary currents. These potentials can be computed and are assumed to be known.

Correspondingly, the unknown true potentials $w_j(x) = u_j(x) + \varepsilon v_j(x) + o(\varepsilon)$ for the actual conductivity σ satisfy the equations

$$\nabla \cdot \sigma \nabla (u_j + \varepsilon v_j) = 0$$

with the same boundary currents as u_j.

According to the discussion in the previous section, using acoustic delta-perturbations (real or synthesized), we can obtain for any point x in the domain Ω the values

$$M^0_{j,k}(x) := \sigma_0(x) \nabla u_j(x) \cdot \nabla u_k(x), \tag{13}$$

which can be computed numerically using the background conductivity σ_0, and

$$M_{j,k}(x) := \sigma(x)\nabla w_j(x) \cdot \nabla w_k(x) = M^0_{j,k} + \varepsilon g_{j,k} + o(\varepsilon), \tag{14}$$

which are obtained by boundary measurements. Now we can forget the acoustic modulation and concentrate on reconstructing $\rho(x)$ (and thus $\sigma(x)$) from the known $M_{j,k}(x)$, or, neglecting higher order terms, from $g_{j,k}(x)$.

Let us rewrite (14) in the following form:

$$\sigma(x)\nabla[u_j(x) + \varepsilon v_j(x)] \cdot \nabla[u_k(x) + \varepsilon v_k(x)] = M^0_{j,k} + \varepsilon g_{j,k} + o(\varepsilon). \tag{15}$$

By subtracting (13) from (15), one obtains the formulas

$$g_{j,k}(x) = \sigma(\nabla u_j \cdot \nabla v_k + \nabla u_k \cdot \nabla v_j) + o(\varepsilon). \tag{16}$$

We will drop the $o(\varepsilon)$ terms in the following calculations. We introduce the new vector fields $U_j = \sqrt{\sigma_0}\nabla u_j$ and $W_j = \sqrt{\sigma}\nabla(u_j + \varepsilon v_j) = U_j + \varepsilon V_j$, so that

$$\nabla \cdot \sqrt{\sigma_0} U_j = 0$$

and

$$\nabla \cdot \sqrt{\sigma} W_j = 0.$$

We would like to find W_j. The last equation can be rewritten, taking into account that, up to $o(\varepsilon)$ terms, $\sqrt{\sigma} \approx \sqrt{\sigma_0}\big(1 + \frac{1}{2}\varepsilon\rho\big)$ and $\ln\sigma = \ln\sigma_0 + \varepsilon\rho$, as follows:

$$\nabla \cdot \sqrt{\sigma_0}(1 + \varepsilon\rho/2)(U_j + \varepsilon V_j) = 0$$

or

$$\nabla \cdot (U_j + \varepsilon V_j) + \tfrac{1}{2}(U_j + \varepsilon V_j) \cdot \nabla(\ln\sigma + \varepsilon\rho) = 0.$$

By collecting the terms of the zero and first order in ε, we obtain

$$\nabla \cdot U_j + \tfrac{1}{2} U_j \cdot \nabla \ln\sigma = 0$$

and

$$\nabla \cdot V_j + \tfrac{1}{2} U_j \cdot \nabla\rho + \tfrac{1}{2} V_j \cdot \nabla \ln\sigma = 0$$

or

$$\nabla \cdot V_j + \tfrac{1}{2} V_j \cdot \nabla \ln\sigma = -\tfrac{1}{2} U_j \cdot \nabla\rho.$$

Equivalently,

$$\nabla \cdot \sqrt{\sigma} V_j = -\tfrac{1}{2}\sqrt{\sigma} U_j \cdot \nabla\rho.$$

With this new notation, the measurements can be expressed (neglecting higher order terms) as follows:

$$(U_j + \varepsilon V_j) \cdot (U_k + \varepsilon V_k) = M_{j,k} = M^0_{j,k} + \varepsilon g_{j,k},$$

which leads to

$$U_j \cdot U_k = M^0_{j,k},$$
$$U_j \cdot V_k + U_k \cdot V_j = g_{j,k}.$$

In particular, we arrive at three independent equations for V_j:

$$\begin{aligned} U_1 \cdot V_1 &= g_{1,1}/2 \\ U_2 \cdot V_2 &= g_{2,2}/2 \\ U_1 \cdot V_2 + U_2 \cdot V_1 &= g_{1,2}. \end{aligned} \tag{17}$$

These equations will be our starting point for deriving reconstruction algorithms, as well as uniqueness and stability results.

We consider now the case when the benchmark conductivity (initial conductivity guess) is constant: $\sigma_0(x) \equiv 1$.

3.1. The constant benchmark conductivity $\sigma_0(x) = 1$

We will choose the boundary currents $\frac{\partial}{\partial n}u_j(x)$ to be equal to $n(x) \cdot e_j$, where $n(x)$ is the unit external normal to the boundary and $e_1 = (1, 0)$, $e_2 = (0, 1)$ are the canonical basis vectors. Then for the conductivity $\sigma_0 = 1$, the resulting potentials $u_j(x)$ are equal to x_j, and the fields U_j are equal to e_j:

$$U_j = \nabla u_j = e_j, \qquad j = 1, 2.$$

We thus obtain the formulas

$$\begin{cases} 2\dfrac{\partial v_1}{\partial x_1} + \rho = g_{1,1} \\ 2\dfrac{\partial v_2}{\partial x_2} + \rho = g_{2,2} \\ \dfrac{\partial v_1}{\partial x_2} + \dfrac{\partial v_2}{\partial x_1} = g_{1,2} \end{cases} \tag{18}$$

as well as the equations

$$\Delta v_j = -\frac{\partial}{\partial x_j}\rho, \qquad j = 1, 2. \tag{19}$$

Differentiating equations (18), we obtain

$$\begin{cases} 2\dfrac{\partial^2 v_1}{\partial x_1^2} + \dfrac{\partial}{\partial x_1}\rho = \dfrac{\partial}{\partial x_1}g_{1,1} \\ 2\dfrac{\partial^2 v_1}{\partial x_1 \partial x_2} + \dfrac{\partial}{\partial x_2}\rho = \dfrac{\partial}{\partial x_2}g_{1,1} \\ 2\dfrac{\partial^2 v_2}{\partial x_2^2} + \dfrac{\partial}{\partial x_2}\rho = \dfrac{\partial}{\partial x_2}g_{2,2} \\ 2\dfrac{\partial^2 v_2}{\partial x_1 \partial x_2} + \dfrac{\partial}{\partial x_1}\rho = \dfrac{\partial}{\partial x_1}g_{2,2} \\ \dfrac{\partial^2 v_1}{\partial x_1 \partial x_2} + \dfrac{\partial^2 v_2}{\partial x_1^2} = \dfrac{\partial}{\partial x_1}g_{1,2} \\ \dfrac{\partial^2 v_1}{\partial x_2^2} + \dfrac{\partial^2 v_2}{\partial x_1 \partial x_2} = \dfrac{\partial}{\partial x_2}g_{1,2}. \end{cases} \tag{20}$$

Combining the second, third, and fifth equations in (20), we arrive at

$$0 = \frac{\partial}{\partial x_2}g_{1,1} - 2\frac{\partial}{\partial x_1}g_{1,2} - \frac{\partial}{\partial x_2}g_{2,2} + 2\Delta v_2.$$

Utilizing (19) with $j = 2$ and differentiating with respect to x_2, we obtain

$$\frac{\partial^2}{\partial x_2^2}\rho = \frac{1}{2}\frac{\partial^2}{\partial x_2^2}(g_{1,1} - g_{2,2}) - \frac{\partial^2}{\partial x_1 \partial x_2}g_{1,2}.$$

Similarly,

$$\frac{\partial^2}{\partial x_1^2}\rho = \frac{1}{2}\frac{\partial^2}{\partial x_1^2}(g_{2,2} - g_{1,1}) - \frac{\partial^2}{\partial x_1 \partial x_2}g_{1,2}.$$

Adding the last two equalities, we obtain the Poisson-type equation

$$\Delta\rho = \frac{1}{2}\left(\frac{\partial^2}{\partial x_1^2} - \frac{\partial^2}{\partial x_2^2}\right)(g_{2,2} - g_{1,1}) - 2\frac{\partial^2}{\partial x_1 \partial x_2}g_{1,2} \tag{21}$$

for the unknown function ρ. Note that all expressions on the right-hand side are obtained from the measured data and that by our assumption ρ satisfies the zero Dirichlet condition at the boundary.

This reduction clearly allows for the algorithmic reconstruction, as well as proving (under appropriate smoothness assumptions on σ) the local uniqueness and Lipschitz stability of reconstruction (see section 4).

3.2. A parametrix solution for smooth benchmark conductivity $\sigma_0(x)$

We would like to now present a sometimes useful observation for the situation when the benchmark conductivity σ_0 is smooth, but not necessarily constant (e.g., a standard EIT reconstruction would provide such an approximation). In this case, we will find a parametrix solution, i.e. determine $\sigma(x)$ up to smoother terms.

As has already been discussed, the perturbation εv_j of the potential u_j satisfies the equation

$$\nabla \cdot \sigma_0 \nabla v_j = -\sigma_0 \nabla u_j \cdot \nabla \rho.$$

Since σ is smooth and non-vanishing, up to smoother terms, we can write

$$\Delta v_j \approx -\nabla u_j \cdot \nabla \rho$$

and

$$v_j \approx -(\nabla u_j \cdot \nabla)(\Delta^{-1}\rho)$$

where Δ^{-1} is the inverse to the Dirichlet Laplacian in Ω. Again up to smoother terms, we have

$$\begin{aligned} U_k \cdot V_j &= \sqrt{\sigma}\nabla u_k \cdot \sqrt{\sigma}(\rho/2\nabla u_j + \nabla v_j) \\ &= \sigma\rho/2\nabla u_k \cdot \nabla u_j + \sigma(\nabla u_k \cdot \nabla)(\nabla u_j \cdot \nabla)\Delta^{-1}\rho. \end{aligned}$$

The latter expression is symmetric up to smoothing terms and equations (17) can be rewritten as

$$\begin{aligned} U_1 \cdot V_1 &= g_{1,1}/2 \\ U_2 \cdot V_2 &= g_{2,2}/2 \\ U_1 \cdot V_2 &= g_{1,2}/2 + \text{ a smoother term} \\ U_2 \cdot V_1 &= g_{1,2}/2 + \text{ a smoother term.} \end{aligned}$$

Under such an approximation, assuming that the currents ∇u_1 and ∇u_2 are not parallel, which is known to be possible to achieve [2], one can recover εV_j at each point x. Therefore, (more) accurate solutions $W_j = U_j + \varepsilon V_j$ can be found. We note that $\nabla \cdot \sqrt{\sigma} W_j = 0$ and so

$$W_j \cdot \nabla \ln \sigma = -2\nabla \cdot W_j.$$

On the other hand, since $W_j = \sqrt{\sigma}\nabla(u_j + \varepsilon v_j)$, we have

$$\nabla \times \frac{W_j}{\sqrt{\sigma}} = 0.$$

This can be rewritten as

$$W_j \times \nabla \ln \sigma = -2\nabla \times W_j$$

or

$$W_j^{\perp} \cdot \nabla \ln \sigma = -2\nabla \times W_j,$$

where $W_j^{\perp}$ is the vector obtained from W_j by the counter-clockwise 90° rotation (i.e. $W_j^{\perp} \cdot W_j = 0$ and $\left|W_j^{\perp}\right| = |W_j|$).

Since for each $j = 1, 2$ vectors W_j and $W_j^\perp$ form an orthogonal basis, one has

$$\nabla \ln \sigma = -\frac{2}{|W_j|^2}(W_j^\perp(\nabla \times W_j) + W_j(\nabla \cdot W_j)),$$

and thus

$$\Delta \ln \sigma = -\mathrm{div}\frac{2}{|W_j|^2}\big(W_j^\perp(\nabla \times W_j) + W_j(\nabla \cdot W_j)\big).$$

We compute now $\ln \sigma$ by taking the average of the two values of j and then solving the Poisson equation

$$\Delta \ln \sigma = -\mathrm{div}\sum_{j=1}^{2}\frac{2}{|W_j|^2}(W_j^\perp\big(\nabla \times W_j) + W_j(\nabla \cdot W_j)\big).$$

It is interesting to note that this solution reduces to (21) when $\sigma = 1$, although (21) holds exactly, not just up to smoother terms.

4. Uniqueness and stability

In this section, we assume that $\sigma \in C^{1,\alpha}(\Omega)$, and thus ρ belongs to this space as well (recall that ρ also vanishes in a fixed neighborhood of $\partial\Omega$).

The questions of uniqueness and stability in the situation close to ours have already been addressed in [5, 7], so we will be brief here. Although considerations of [5, 7] were provided in 2D, the conclusion in our situation works out the same way in 3D if three currents are used.

The standard elliptic regularity [13] implies the following.

Proposition 1 [5, 7]**.**

(1) The data $g_{i,j}$ in (14) determine the conductivity $\sigma = 1 + \rho$ uniquely.

(2) The mappings $\rho(x) \mapsto \{g_{i,j}(x)\}$ of the space $C_0^{1,\alpha}(\overline{V})$, where V is a compact sub-domain of Ω, are Fréchet differentiable.

This justifies our formal linearization near the benchmark conductivity σ_0. Now, the calculations of section 3.1 provide explicit formulas for the Fréchet derivative of the proposition[4]. In particular,

$$\begin{aligned}\frac{\partial}{\partial x_1}\rho &= \frac{1}{2}\frac{\partial}{\partial x_1}(g_{2,2} - g_{1,1}) - \frac{\partial}{\partial x_2}g_{1,2},\\ \frac{\partial}{\partial x_2}\rho &= \frac{1}{2}\frac{\partial}{\partial x_2}(g_{1,1} - g_{2,2}) - \frac{\partial}{\partial x_1}g_{1,2}.\end{aligned} \tag{22}$$

These formulas and vanishing of ρ near $\partial\Omega$ show that the norm of ρ in $C^{1,\alpha}$ can be estimated from the above by such norms of the functions $\{g_{11}, g_{12}, g_{22}\}$. In other words, the Fréchet derivative of the mapping

$$\rho \mapsto \{g_{11}, g_{12}, g_{22}\} \tag{23}$$

is a semi-Fredholm operator with zero kernel. Then the standard implicit function-type argument shows (see, e.g., [19, corollary 5.6, chapter I]) that (23) is an immersion. This proves local uniqueness and stability for the nonlinear problem (the analogous result is obtained in 2D in [5]).

[4] In fact, these formulas easily imply the statement of the proposition in our particular case.

Moreover, since our algorithms start with inverting the Fréchet derivative, this reduces near the constant conductivity the nonlinear problem to the one with an identity plus a contraction operator. This explains why the fixed point iterations in the following sections converge so nicely.

The 3D case with three currents works the same way. Similar to how it is done in section 3.1, for a constant conductivity benchmark σ_0, one can always find boundary currents that produce fields $U_j = e_j$, $j = 1, 2, 3$. Then, as explained in section 6, one obtains an elliptic system of equations (see equation (26)) for reconstructing $\rho(x)$.

5. Numerical examples in 2D

We will now illustrate the properties of our algorithm on several numerical examples in 2D. Each simulation involves several steps. First we model the direct problem as follows. For a given phantom of σ and a fixed boundary current J, we solve equation (1) in the unit square $[-1, 1] \times [-1, 1]$, and (for a chosen weight function I) we compute the unperturbed boundary functionals $M_{I,J}^{\text{unperturbed}}$:

$$M_{I,J}^{\text{unperturbed}} := \int_{\partial\Omega} u(z) I(z)\, \mathrm{d}z. \tag{24}$$

Next, for a set of values of t and z, we perturb σ by multiplying it by $\exp(\eta_{t,z}(x))$ with $\eta_{t,z}(x)$ proportional to the propagating acoustic pulse $W_{t,z}$ given by equation (7). (In simulation we used a mollified version of the delta function, which corresponds to a transducer with a finite bandwidth.) For each perturbed σ we again solve equation (1), obtain the solution $u^{\text{perturbed}}$, and compute functionals,

$$M_{I,J}^{\text{perturbed}}(t, z) := \int_{\partial\Omega} u^{\text{perturbed}}(z) I(z)\, \mathrm{d}z. \tag{25}$$

Finally, the difference of $M_{I,J}^{\text{perturbed}}(t, z)$ and $M_{I,J}^{\text{unperturbed}}$ yields the values of the functionals $M_{I,J}(t, z)$ given by equation (8) which we consider the simulated measurements and the starting point for solving the inverse problems. In some of our numerical experiments, we add values of a random variable to these functions to simulate the noise in the measurements.

The advantage of computing $M_{I,J}(t, z)$ as the difference of two solutions (as opposed to obtaining it from the linearized equation (8)) consists in eliminating the chance of committing 'an inverse crime'. However, since the subtraction of two numerically computed functions that differ very little can significantly amplify the relative error, our forward solver has to be very accurate. In order to achieve high accuracy, we approximated the potentials in the square by Fourier series and used the fast Fourier transforms (FFT) to compute the corresponding differential operators. In turn, the application of the FFTs allowed us to use fine discretization grids (513×513), which, in combination with smoothing of the simulated $\sigma(x)$, yields the desired high accuracy. (Such algorithms combining the use of global bases (such as the trigonometric basis utilized here) with enforcing the equation in the nodes of the computational grid are called *pseudospectral* [11]; they are very efficient when the computational domain is simple (e.g. a square) and the coefficients of the equation are smooth.)

After the measurement data have been simulated, the inverse problem of AET is solved by reconstructing functions $M_{i,j}$ (see equation (9)) from $M_{I,J}(t, z)$ (synthesis step), and by applying the methods of section 3 to reconstruct $\varepsilon\rho(x)$ (i.e. the difference between the true conductivity and the benchmark σ_0).

Our phantom (i.e. simulated $\ln\sigma(x)$) consists of several slightly smoothed characteristic functions of circles, shown in figures 1(a) and 5(a). (A more detailed description is presented

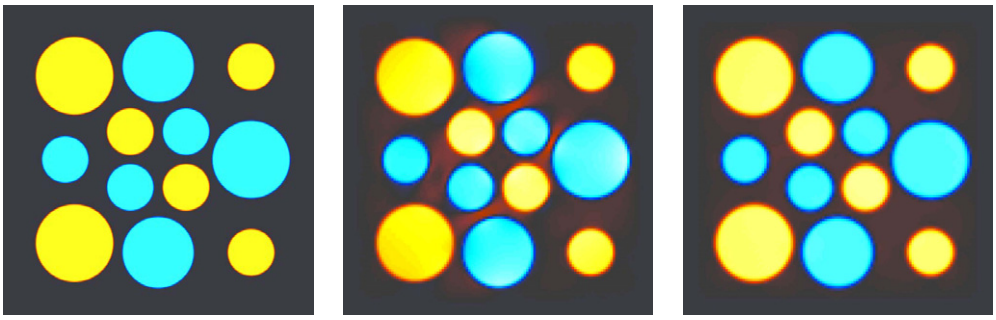

(a) (b) (c)

Figure 1. Reconstruction in 2D from noiseless data: (a) phantom, (b) iteration 0, (c) iteration 1.

in the appendix.) Smoothing guarantees that the phantom is fully resolved on the fine discretization grid we use during the forward computations, which helps to ensure its high accuracy (several correct decimal digits). The characteristic functions comprising the phantom are weighted with weights 1 or -1, so that $\sigma(x)$ varies between e and e^{-1}. Thus, the conductivity deviates far from the initial guess $\sigma_0 \equiv 1$. The current I_1 equals 1 and -1 on the right and left sides of the square, respectively; it vanishes on the horizontal sides. The current I_2 coincides with I_1 rotated 90° counterclockwise.

The simulated sources of the propagating spherical acoustic fronts are centered on a circle of the diameter slightly larger than the diagonal of the square domain. There were 256 simulated transducers uniformly distributed over the circle. Each transducer produced 257 spherical fronts of the radii ranging from 0 to the diameter of the circle. For each front radius t_l and center z_m, the perturbed σ was modeled, the nonlinear direct $M_{I_j,I_k}(t_l, z_m)$, $j, k = 1, 2$, were computed as explained at the beginning of this section. In the first of our experiments, these accurate data were used as a starting point of the reconstruction. In the second experiment, they were perturbed by a 50% (in the L^2 norm) noise.

The first step of the reconstruction is synthetic focusing, i.e. finding the values $M_{j,k}(x)$ from $M_{I_j,I_k}(t, z)$, $j, k = 1, 2$. In order to give the reader a better feeling of synthetic focusing, we present in figure 2 a picture of a propagating spherical acoustic front (part (a)), and an approximation to a delta function located at the point (0.2, 0.4) obtained as a linear combination of such fronts (part (b)). Figure 2(c) shows the same function as in part (b) with a modified gray scale that corresponds to the lower 10% of that function's range, and thus allows one to see small details invisible in part (b). These figures are provided for demonstration purposes only, since in our algorithm reconstruction of the values $M_{j,k}(x)$ from $M_{I_j,I_k}(t, z)$ is performed by applying the 2D exact filtration backprojection formula to the latter function (we used the exact reconstruction formula from [17], but other options are also available). On a 129 × 129 grid, this computation takes a few seconds. Since the formula is applied to the data containing the derivative of the delta function, the differentiation appearing in the TAT inversion formula (e.g., [1, 10, 15, 17]) is not needed, and the reconstruction instead of being slightly unstable, has a smoothing effect (this is why we obtain high-quality images with such a high level of noise).

In the second step of the reconstruction, the functions $M^0_{j,k}(x)$ are computed using the knowledge of the benchmark conductivity σ_0, and the values of $g_{j,k}(x)$ are obtained by comparing $M_{j,k}(x)$ and $M^0_{j,k}(x)$. Then the first approximation to ρ (we will call it iteration 0) is obtained by solving equation (21). The right-hand side of this equation is computed by finite

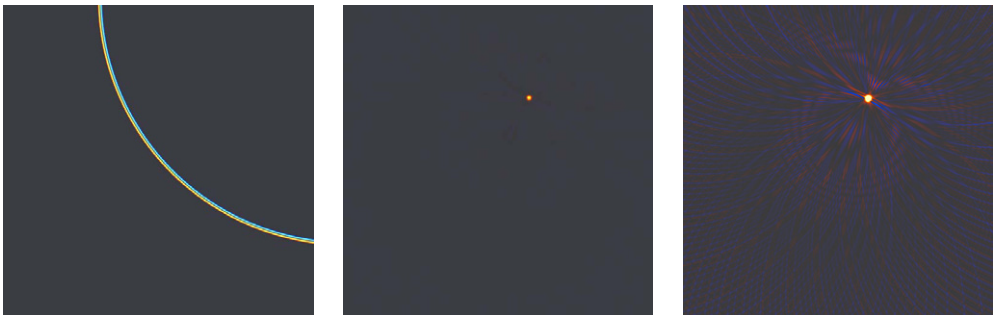

(a) (b) (c)

Figure 2. (a) Propagating acoustic front, (b) the result of focusing at the point (0.2, 0.4), (c) the same as (b) with the gray scale showing the lower 10% of the range of the function.

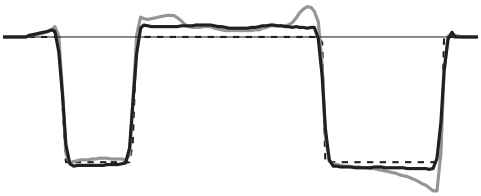

Figure 3. Horizontal central cross section (accurate data): the dashed line denotes the phantom, the gray line represents iteration 0, and the thick black solid line represents iteration 1.

differences, and then the Poisson equation in a square is solved by the decomposition in 2D Fourier series. The computation is extremely fast due to the use of the FFT. More importantly, since the differentiation of the data is followed by the application of the inverse Laplacian, this step is completely stable (the corresponding pseudodifferential operator is of order zero), and no noise amplification occurs.

Finally, we attempt to improve the reconstruction by accepting the reconstructed σ as a new benchmark conductivity and by applying to the data the parametrix algorithm of the previous section. We call this computation iteration 1.

Figure 1 demonstrates the result of such a reconstruction from data without noise. Part (a) of the figure shows the phantom, and parts (b) and (c) present the results of iterations 0 and 1, on the same gray-level scale. The profiles of the central horizontal cross sections of these functions are shown in figure 3. One can see that even the iteration 0 produces quite a good reconstruction; iteration 1 removes some of the artifacts, and improves the shape of circular inclusions. For the convenience of the reader, we summarize the parameters of this simulation in the appendix.

Figures 4, 5 and 6 present the results of the reconstruction from noisy data. In this simulation, we used the phantom from the previous example, and we added to the data 50% (in the L^2 norm) noise. The first step of the reconstruction (synthetic focusing) is illustrated in figure 4. Parts (a) and (c) of this figure show accurate values of the functionals $M_{1,1}(x)$ and $M_{1,2}(x)$. Parts (b) and (d) present the reconstructed values of these functionals obtained by synthetic focusing. One can see the effect of smoothing mentioned earlier in this section: the level of noise in the reconstructions is much lower than the level of noise in the simulated measurements. The images reconstructed from $M_{i,j}(x)$ in the second step are presented in

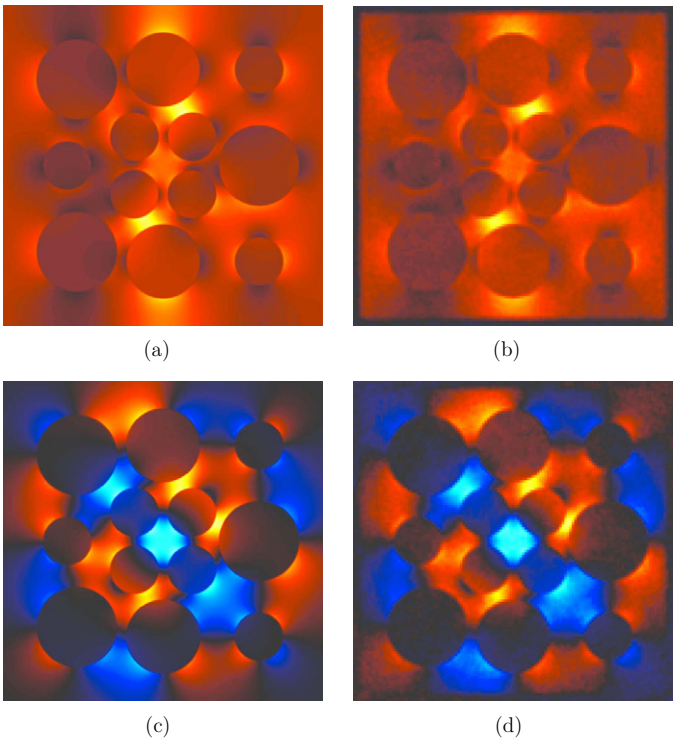

Figure 4. Functionals $M_{i,j}$: (a) original $M_{1,1}$, (b) $M_{1,1}$ reconstructed from data contaminated by 50% noise; (c) original $M_{1,2}$, (d) $M_{1,2}$ reconstructed from data contaminated by 50% noise.

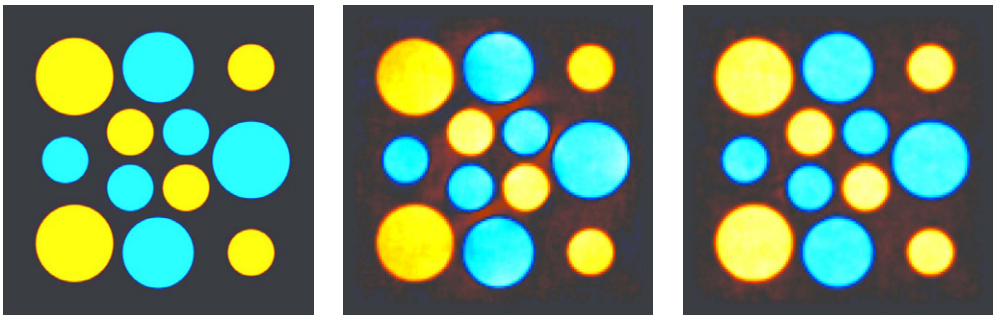

Figure 5. Reconstruction from the data contaminated by a 50% noise: (a) phantom, (b) iteration 0, (c) iteration 1.

figures 5 and 6. The meaning of the images is the same as those in figures 1 and 3. The level of noise in these images is comparable to that in the reconstructed $M_{i,j}$'s. To summarize, our method can reconstruct high-quality images from the data contaminated by a strong noise since the first step of the method is an application of a smoothing operator, and the second step uses the parametrix.

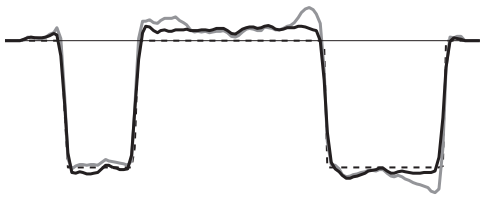

Figure 6. Horizontal central cross section (noisy data): the dashed line denotes the phantom, the gray line represents iteration 0, and the thick black solid line represents iteration 1.

(a) (b) (c)

Figure 7. Reconstruction from noiseless data: (a) phantom, (b) iteration 0, (c) iteration 4.

Finally, figure 7 shows the reconstruction of a phantom containing objects with corners. The phantom is shown in part (a) of the figure, part (b) demonstrates iteration 0, and part (c) presents the result of the iterative use of the parametrix method described in the previous section (iteration 4 is shown).

6. Reconstruction in 3D

Let us now consider the reconstruction problem in 3D. The 3D case is very important from the practical point of view, since propagation of electrical currents is essentially three dimensional. Indeed, unlike x-rays or high-frequency ultrasound, currents cannot be focused to stay in a two-dimensional slice of the body. However, while successful 3D reconstructions were reported [7], the theoretical foundations of the 3D case have not been completed yet, due to some analytic difficulties arising in other approaches. In contrast, the present approach easily generalizes to 3D, and leads to a fast, efficient, and robust reconstruction algorithm.

We will assume that three different currents I_j, $j = 1, 2, 3$, are used, and that the boundary values of the corresponding potentials w_j, $j = 1, 2, 3$, are measured on $\partial\Omega$. Similar to the 2D case presented in section 2, by perturbing the medium with a perfectly focused acoustic beam (no matter whether such measurements are real or synthesized), one can recover at each point x within Ω the values of the functionals $M_{i,j}(x)$, $i, j = 1, 2, 3$, where, as before,

$$M_{i,j}(x) = \sigma(x)\nabla w_i(x) \cdot \nabla w_j(x).$$

Our goal is to reconstruct the conductivity $\sigma(x)$ from $M_{i,j}(x)$. As before, we will assume that $\sigma(x)$ is a perturbation of a known benchmark conductivity $\sigma_0(x)$, i.e. $\sigma(x) = \sigma_0(x)(1 + \varepsilon\rho(x))$, and that the values of potentials $w_j(x)$ are the perturbations of known

potentials $u_j(x)$ corresponding to $\sigma_0(x)$:

$$w_j(x) = u_j(x) + \varepsilon v_j(x) + o(\varepsilon).$$

Now the functionals $M_{j,k}(x)$ are related to the known unperturbed values $M^0_{j,k}(x)$ and measured perturbations $g_{j,k}(x)$ by equations (14) and (13).

As was performed in section 3, we introduce vector fields $U_j = \sqrt{\sigma_0}\nabla u_j$ and $W_j = \sqrt{\sigma}\nabla(u_j + \varepsilon v_j) = U_j + \varepsilon V_j$, and proceed to derive the following six equations:

$$\begin{aligned}
U_1 \cdot V_1 &= g_{1,1}/2\\
U_2 \cdot V_2 &= g_{2,2}/2\\
U_3 \cdot V_3 &= g_{3,3}/2\\
U_1 \cdot V_2 + U_2 \cdot V_1 &= g_{1,2}\\
U_1 \cdot V_3 + U_3 \cdot V_1 &= g_{1,3}\\
U_2 \cdot V_3 + U_3 \cdot V_2 &= g_{2,3}.
\end{aligned}$$

One can obtain a useful approximation to $\rho(x)$ by assuming $\sigma_0 = 1$, and by selecting unperturbed currents so that the potentials $u_j(x) = x_j$. Then, by repeating derivations of section 3.1, one obtains the following three formulas:

$$\begin{cases}
\left(\dfrac{\partial^2}{\partial x_1^2} + \dfrac{\partial^2}{\partial x_2^2}\right)\rho = \dfrac{1}{2}\left(\dfrac{\partial^2}{\partial x_1^2} - \dfrac{\partial^2}{\partial x_2^2}\right)(g_{2,2} - g_{1,1}) - 2\dfrac{\partial^2}{\partial x_1 \partial x_2} g_{1,2}\\
\left(\dfrac{\partial^2}{\partial x_1^2} + \dfrac{\partial^2}{\partial x_3^2}\right)\rho = \dfrac{1}{2}\left(\dfrac{\partial^2}{\partial x_1^2} - \dfrac{\partial^2}{\partial x_3^2}\right)(g_{3,3} - g_{1,1}) - 2\dfrac{\partial^2}{\partial x_1 \partial x_3} g_{1,3}\\
\left(\dfrac{\partial^2}{\partial x_2^2} + \dfrac{\partial^2}{\partial x_3^2}\right)\rho = \dfrac{1}{2}\left(\dfrac{\partial^2}{\partial x_2^2} - \dfrac{\partial^2}{\partial x_3^2}\right)(g_{3,3} - g_{2,2}) - 2\dfrac{\partial^2}{\partial x_2 \partial x_3} g_{2,3}.
\end{cases} \tag{26}$$

We note that by using the first of the above equations, one can compute an approximation to $\rho(x)$ by solving a set of 2D Poisson equations (one for each fixed value of x_3), since boundary values of $\rho(x)$ are equal to 0. This leads to a slice-by-slice 3D reconstruction, which is based only on the values of $g_{1,1}$, $g_{2,2}$ and $g_{1,2}$, and therefore can be performed by using a single pair of currents.

One can obtain better images by using all three currents and doing a fully 3D reconstruction. Namely, summing equations (26) yields the values of $2\Delta\rho$ on the left-hand side. Then one can solve the 3D Poisson equation with the zero boundary conditions to recover the conductivity.

One can expect that, as in 2D, this approach would work well for $\sigma(x)$ close to $\sigma_0 = 1$. However, as demonstrated by our numerical experiments presented in section 7, the results remain quite accurate when $\sigma(x)$ varies significantly across Ω. Moreover, a simple fixed point iteration based on the repeated use of formulas (26) exhibits a rapid convergence to the correct image.

7. Numerical examples in 3D

In this section we present the results of 3D reconstructions from simulated data. Unfortunately, a complete modeling of the forward problem in 3D (i.e. computation of the perturbations corresponding to the propagating acoustic spherical fronts) would require the solution of $\mathcal{O}(n^3)$ 3D divergence equations. This task is computationally too expensive. Therefore, unlike in our 2D simulations, we resort to modeling the values of the functionals $M_{i,j}(x)$ on a $257 \times 257 \times 257$ Cartesian grid, using formulas (26). These values correspond to the data

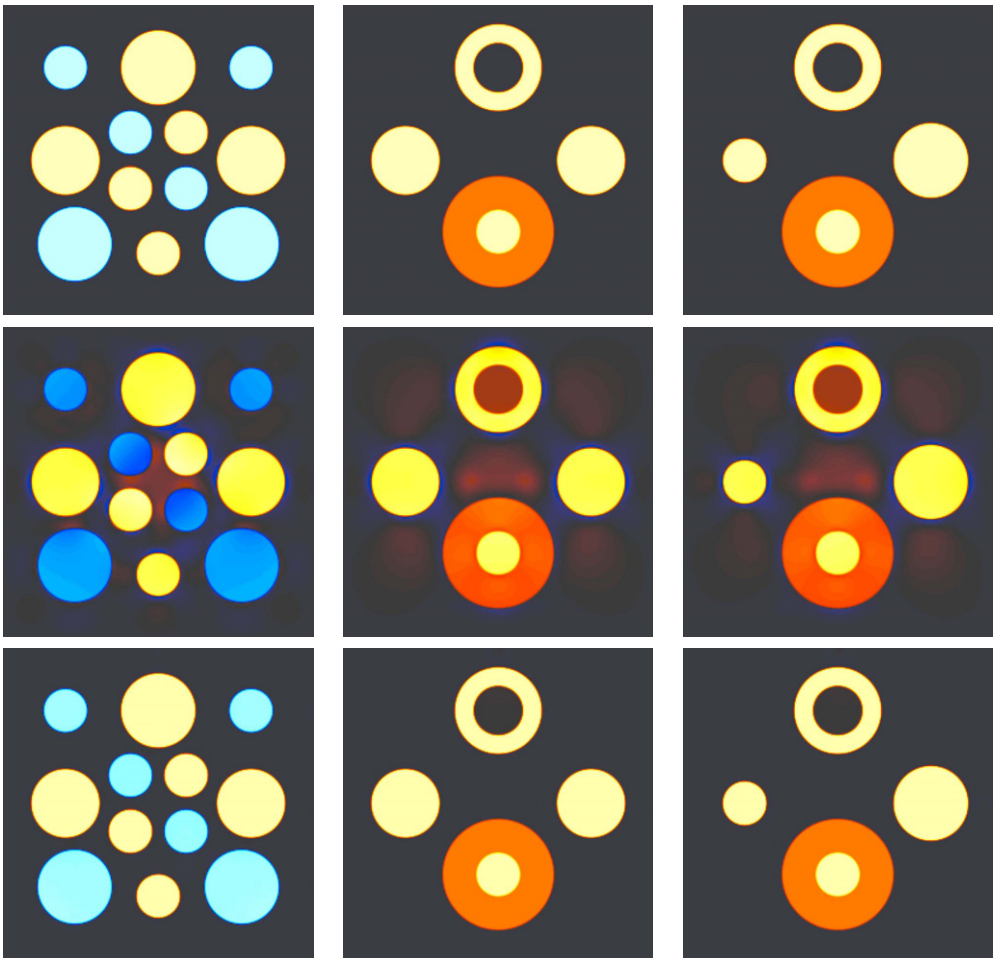

Figure 8. 3D reconstruction from noiseless data. First row: phantom (a) Ox_1x_2 cross section, (b) Ox_1x_3 cross section, (c) Ox_2x_3 cross section. Second row: iteration 0. Third row: iteration 4.

that would be measured if perfectly focused, infinitely small perturbations were applied to the conductivity. Thus, in this section we only test the second step of our reconstruction techniques. However, as mentioned before, if the real data were available, the first step (synthetic focusing) could be performed by applying any of the several available stable versions of thermoacoustic inversion, and the feasibility of this step was clearly demonstrated in the 2D sections of this paper, as well as in [16].

In our first simulation, we used the noiseless values of $M_{i,j}(x)$ and reconstructed the conductivity on a $257 \times 257 \times 257$ grid. The first row of figure 8 shows three 2D cross sections of a 3D phantom. The result of approximate inversion (using three currents, as described in section 6) is presented in the second row of the figure. Finally, the last row shows the result of the iterative use of formulas (26), where ρ now represents the difference between the previous and the updated approximations to the conductivity. The third row demonstrates iteration 4. In addition, figure 9 shows the trace along a diagonal cross section in the Ox_1x_2 plane (that

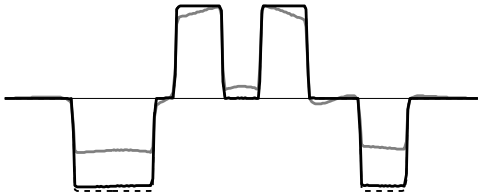

Figure 9. Diagonal cross section (noiseless data): the dashed line denotes the phantom, the gray line represents iteration 0, and the thick black solid line represents iteration 4.

corresponds to the diagonals of images presented in column (a) of figure 8). We summarize details of this simulation in the appendix.

In our second 3D experiment, we utilized the same phantom, but as the data used only a subset of the values of $M_{i,j}$ corresponding to a coarser $129 \times 129 \times 129$ grid, the latter coarse grid was also used to discretize the reconstructed conductivity. We also added to the data 10% (in the L^2 norm) noise. Figure 10 presents the cross sections of a 3D phantom and the reconstructions obtained using three currents, on the same gray-level scale. The meaning of the subfigures is the same as those in figure 8. Finally, figure 11 shows the trace along the diagonal cross sections of the images in the Ox_1x_2y plane.

In both these examples, the iteration 0 yields the good qualitative reconstruction of the conductivity in spite of the fact that the latter varies from e^{-1} to e^1, and thus differs strongly from the benchmark guess $\sigma_0 = 1$. The subsequent iterations demonstrate fast convergence to the correct values of $\sigma(x)$.

8. Final remarks and conclusions

We have shown that the proposed algorithm works stably and yields the quality reconstructions of the internal conductivity. It does not require physical focusing of ultrasound waves and replaces it with the synthetic focusing procedure, which can be implemented using one of the known thermoacoustic imaging inversion methods (e.g., time reversal or inversion formulas). Under appropriate smoothness conditions on the conductivity, our analysis leads to the proof of local uniqueness and stability of the reconstruction. However, since this conclusion has already been made in 2D in [5, 7], we only presented a sketch of the proof.

Some additional remarks are as follows.

(1) Using the propagating spherical fronts of the type considered in this text (equation (7)) is advantageous since in this case synthetic focusing is a smoothing operator, and thus the whole reconstruction procedure is more stable with respect to errors than the one that starts with focused data.

(2) Reconstructions can be performed with single, two, or (in 3D) three currents. A single current procedure was the one we used initially in 2D [16, 18]. It works, but requires solving a transport equation for the conductivity. When such a procedure is used, errors arising due to the noise and/or under-resolved interfaces tend to propagate along the current lines, thus reducing the quality of the reconstructed image. The two-current approach in 2D is elliptic and thus does not propagate errors. The two-current slice-by-slice reconstruction in 3D is also possible, but the use of three currents seems to produce better results.

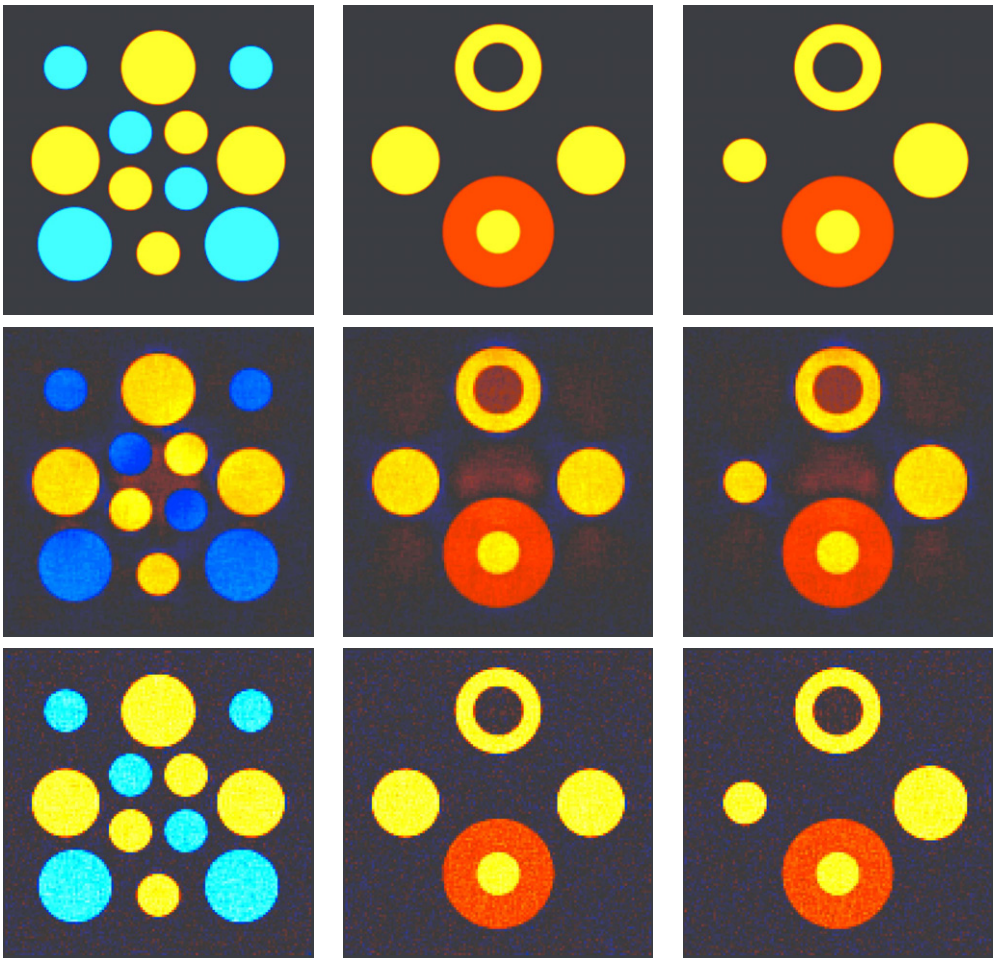

(a) (b) (c)

Figure 10. 3D reconstruction from noisy data on a coarser grid. First row: phantom (a) Ox_1x_2 cross section, (b) Ox_1x_3 cross section, (c) Ox_2x_3 cross section. Second row: iteration 0; third row: iteration 4.

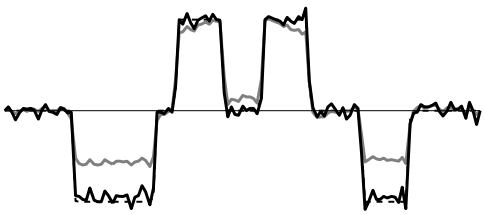

Figure 11. Diagonal cross section of reconstructions obtained from noisy data on a coarser gird: the dashed line denotes the phantom, the gray line represents iteration 0, and the thick black solid line represents iteration 4.

The results of this work were presented at the conferences 'Integral Geometry and Tomography', Stockholm, Sweden, August 2008; 'Mathematical Methods in Emerging Modalities of Medical Imaging', BIRS, Banff, Canada, October 2009; 'Inverse Transport Theory and Tomography', BIRS, Banff, May 2010; 'Mathematics and Algorithms in Tomography' Oberwolfach, April 2010, and 'Inverse problems and applications', MSRI, Berkeley, August 2010. Brief reports have appeared in [16, 18].

Acknowledgments

The work of both the authors was partially supported by the NSF DMS grant 0908208; the paper was written while they were visiting MSRI. The work of PK was also partially supported by the NSF DMS grant 0604778 and by the Award no KUS-C1-016-04, made to IAMCS by the King Abdullah University of Science and Technology (KAUST). The authors express their gratitude to NSF, MSRI, KAUST, and IAMCS for the support. Thanks also go to G Bal, E Bonnetier, J McLaughlin, L V Nguyen, L Wang, and Y Xu for helpful discussions and references. Finally, we are grateful to the referees for suggestions and comments that helped to significantly improve the paper.

Appendix

In order to make it easier for the reader to repeat our simulations, we summarize in this section details of some of our numerical experiments.

In the first two of the 2D simulations described in section 5, we use a 2D phantom in the form of a linear combination of 12 smoothed characteristic functions of disks with radii r_j^{in} and centers x_j:

$$f(x) = \sum_{j=1}^{12} \alpha_j h\big(|x - x_j|, r_j^{\text{in}}, r_j^{\text{out}}\big), \qquad x_j = (x_{j,1}, x_{j,2}),$$

where

$$h(r, r_j^{\text{in}}, r_j^{\text{out}}) = \begin{cases} 1, & r \leqslant r_j^{\text{in}} \\ 0, & r \geqslant r_j^{\text{out}} \\ \exp\left[2\dfrac{r_j^{\text{out}} - r_j^{\text{in}}}{r - r_j^{\text{out}}} \exp\left(\dfrac{r_j^{\text{out}} - r_j^{\text{in}}}{r_j^{\text{in}} - r}\right)\right], & r_j^{\text{in}} < r < r_j^{\text{out}}, \end{cases}$$

and the values of α_j, $x_{j,1}$, $x_{j,2}$, r_j^{in}, and r_j^{out} are given in table 1. All the smoothed disks lie within the square computational domain $[-1, 1] \times [-1, 1]$. The forward problem was computed on a fine 513×513 grid. We simulated propagating spherical fronts generated by 256 transducers equally spaced on the circle of radius 1.6 centered at the origin. For each transducer we simulated 257 spherical fronts of varying radii. The reconstruction was performed on the coarser 129×129 computational grid, from the data corresponding to two currents. In the first experiment, we used the noiseless data; in the second one, we added to the simulated values the $M_{I,J}(t, z)$ values of a random variable modeling the noise of intensity 50% of the signal in the L^2 norm. The results of these simulations are described in section 5.

In section 7, we utilized a 3D phantom represented by a linear combination of 16 smoothed characteristic functions of balls with radii r_j^{in} and centers x_j:

$$f(x) = \sum_{j=1}^{16} \alpha_j h\big(|x - x_j|, r_j^{\text{in}}, r_j^{\text{out}}\big), \qquad x_j = (x_{j,1}, x_{j,2}, x_{j,3}),$$

Table 1. Parameters of the 2D phantom.

j	$x_{j,1}$	$x_{j,2}$	r_j^{out}	r_j^{in}	α_j
1	−0.54	0.54	0.26	0.24	1
2	0.00	0.60	0.24	0.22	−1
3	0.60	0.60	0.16	0.14	1
4	−0.60	0.00	0.16	0.14	−1
5	0.60	0.00	0.26	0.24	−1
6	−0.54	−0.54	0.26	0.24	1
7	0.00	−0.60	0.24	0.22	−1
8	0.60	−0.60	0.16	0.14	1
9	0.18	0.18	0.16	0.14	−1
10	0.18	−0.18	0.16	0.14	1
11	−0.18	0.18	0.16	0.14	1
12	−0.18	−0.18	0.16	0.14	−1

Table 2. Parameters of the 3D phantom.

j	$x_{j,1}$	$x_{j,2}$	$x_{j,3}$	r_j^{out}	r_j^{in}	α_j
1	−0.615	−0.54	0	0.26	0.22	0.5
2	−0.6	0	0	0.24	0.20	1
3	0.6	0.6	0	0.16	0.12	0.5
4	0	−0.6	0	0.16	0.12	1
5	0	0.6	0	0.26	0.22	1
6	−0.54	−0.54	0	0.26	0.22	0.5
7	−0.6	0	0	0.24	0.20	1
8	−0.6	0.6	0	0.16	0.12	0.5
9	0.18	0.18	0	0.16	0.12	1
10	−0.18	0.18	0	0.16	0.12	0.5
11	0.18	−0.18	0	0.16	0.12	0.5
12	−0.18	−0.18	0	0.16	0.12	1
13	0	0	0.6	0.18	0.14	−1
14	0	0	0.6	0.30	0.26	1
15	0	0	−0.46	0.38	0.34	0.5
16	0	0	−0.46	0.16	0.12	0.5

the values of α_j, $x_{j,1}$, $x_{j,2}$, $x_{j,3}$, r_j^{in}, and r_j^{out} are given in table 2. In our 3D simulations, we had to assume that the values $M_{i,j}(x)$ are known. We modeled these values by using the above-mentioned phantom, in combination with three boundary current profiles. In the case of the constant conductivity, these boundary currents would produce potentials equal to x_j, $j = 1, 2, 3$. We modeled the direct problem using the $257 \times 257 \times 257$ computational grid corresponding to the cube $[-1, 1] \times [-1, 1] \times [-1, 1]$. In the first of our 3D experiments, the reconstruction was performed on the same grid from the noiseless data. In the second experiment, the reconstruction was performed on a coarser $129 \times 129 \times 129$ grid from the data contaminated by a 10% noise (in the L^2 norm). The results of these reconstructions are described in section 7.

References

[1] Agranovsky M, Kuchment P and Kunyansky L 2009 On reconstruction formulas and algorithms for the thermoacoustic and photoacoustic tomography *Photoacoustic Imaging and Spectroscopy* ed L H Wang (Boca Raton, FL: CRC Press) Chapter 8, pp 89–101

[2] Alessandrini G and Nesi V 2001 Univalent σ-harmonic mappings *Arch. Ration. Mech. Anal.* **158** 155–171

[3] Ammari H, Bonnetier E, Capdeboscq Y, Tanter M and Fink M 2008 Electrical impedance tomography by elastic deformation *SIAM J. Appl. Math.* **68** 1557–73

[4] Barber D C and Brown B H 1984 Applied potential tomography *J. Phys. E.: Sci. Instrum.* **17** 723–33

[5] Bonnetier E and Triki F 2010 A stability result for electric impedance tomography by elastic perturbation *Presentation at the Workshop 'Inverse Problems: Theory and Applications' (12 November 2010)* (Berkeley, CA: MSRI)

[6] Borcea L 2002 Electrical impedance tomography *Inverse Problems* **18** R99–136

[7] Capdeboscq Y, Fehrenbach J, de Gournay F and Kavian O 2009 Imaging by modification: numerical reconstruction of local conductivities from corresponding power density measurements *SIAM J. Imag. Sci.* **2/4** 1003–30

[8] Cheney M, Isaacson D and Newell J C 1999 Electrical impedance tomography *SIAM Rev.* **41** 85–101

[9] Cipra B 1994 Shocking images from RPI *SIAM News* **27** 14–5

[10] Finch D and Rakesh 2007 The spherical mean value operator with centers on a sphere *Inverse Problems* **23** S37–50

[11] Fornberg B 1996 *A Practical Guide to Pseudospectral Methods (Cambridge Monographs on Applied and Computational Mathematics* vol 1) (Cambridge: Cambridge University Press)

[12] Gebauer B and Scherzer O 2009 Impedance-acoustic tomography *SIAM J. Appl. Math.* **69** 565–76

[13] Gilbarg D and Trudinger N S 2001 Elliptic partial differential equations of second order *Classics in Mathematics* (Berlin: Springer) (reprint of the 1998 edition)

[14] Hernandez-Figueroa H E, Zamboni-Rached M and Recami E 2008 *Localized Waves* (Hoboken, NJ: IEEE, Wiley)

[15] Kuchment P and Kunyansky L 2008 Mathematics of thermoacoustic tomography *Eur. J. Appl. Math.* **19** 191–224

[16] Kuchment P and Kunyansky L 2010 Synthetic focusing in ultrasound modulated tomography *Inverse Problems Imag.* **4** 665–73

[17] Kunyansky L A 2007 Explicit inversion formulae for the spherical mean Radon transform *Inverse Problems* **23** 373–83

[18] Kunyansky L and Kuchment P 2010 Synthetic focusing in acousto-electric tomography *Oberwolfach Report No 18/2010. Workshop: Mathematics and Algorithms in Tomography (11–17 April) (organized by Martin Burger, Alfred Louis, and Todd Quinto)* pp 44–7 (doi:10.4171/OWR/2010/18)

[19] Lang S 2002 *Introduction to Differentiable Manifolds* 2nd edn (New York: Springer)

[20] Lavandier B, Jossinet J and Cathignol D 2000 Quantitative assessment of ultrasound-induced resistance change in saline solution *Med. Biol. Eng. Comput.* **38** 150–5

[21] Lavandier B, Jossinet J and Cathignol D 2000 Experimental measurement of the acousto-electric interaction signal in saline solution *Ultrasonics* **38** 929–36

[22] Vladimirov V S 1971 *Equations of mathematical physics (Pure and Applied Mathematics* vol 3*)* ed A Jeffrey (New York: Dekker) (Transl. from Russian by A Littlewood)

[23] Wang L V and Wu H 2007 *Biomedical Optics. Principles and Imaging* (New York: Wiley Interscience)

[24] Xu M and Wang L-H V 2006 Photoacoustic imaging in biomedicine *Rev. Sci. Instrum.* **77** 041101

[25] Zhang H and Wang L 2004 Acousto-electric tomography *Proc. SPIE* **5320** 145–9